

All-optical reconfiguration of single silicon-vacancy centers in diamond for non-volatile memories

Received: 1 July 2024

Accepted: 19 June 2025

Published online: 08 July 2025

 Check for updates

Yongzhou Xue¹✉, Xiaojuan Ni², Michael Titze³, Shei Sia Su³, Bohan Wu¹, Liang Zhang¹, Chaohan Cui¹, Saikat Guha¹, Matt Eichenfield^{1,3} & Linran Fan^{1,4}✉

Strain engineering is vital for tuning the optical and spin properties of solid-state color centers, enhancing spin coherence and compensating emission wavelength shift. Here, we develop an all-optical approach to directly modify the local strain of color centers at the nanoscale by migrating the nearby defect. High-power pulsed optical irradiation triggers defect migration, which subsequently leads to the redistribution of the local crystal lattice of the host material. This redistribution alters the strain experienced by nearby color centers. Using silicon-vacancy centers in diamond, we validate this method and demonstrate a ground state splitting enhancement of up to 1.8 THz. Unlike conventional methods, our approach requires no external fields or nanostructure modifications, enabling non-volatile strain control and optical memory functionality across wide temperature ranges. Its local, permanent nature offers a scalable path for enhancing spin coherence in large-scale quantum systems and has potential applications in photonic machine learning.

Group-IV split-vacancy color centers in diamond are garnering increasing interests for their potential in quantum information processing and networking^{1–7}. Critical demonstrations have been performed based on the group-IV centers, such as the memory-enhanced quantum communication and multi-qubit quantum network nodes with built-in error detection ability^{8,9}. For quantum information processing, the coherent time of photons and/or electron spins is arguably the most important parameter to characterize the performance of color centers. For group-IV split vacancy color centers, interaction with the acoustic phonon bath has been identified as the critical factor that reduce the spin coherence time in typical cryogenic environments (~ 4 K)^{3–7}. Without the need to decrease the operating temperature, strain engineering has emerged as a promising method for reducing the interaction between electron spin and the acoustic phonon bath. This approach enhances the ground state (GS) splitting, elevating the energy required for phonon absorption by the emitter well above the

thermal energy at 4 K. Consequently, this leads to an improvement in the spin coherence time^{10–14}. Conventional methods of strain engineering are typically implemented with suspended structures, such as cantilevers^{11,12,14–17}. These approaches have the advantage to achieve continuous and precise tuning, but the fabrication of intricate nanostructures and the application of external electric fields to maintain the strain inevitably increase the complexity of quantum photonic systems based on color centers.

In this work, we present an all-optical approach to control the local strain of color centers, which can be maintained without external fields. We use picosecond pulsed lasers to directly modify the local crystal structure of the host material. We verify this approach with negatively charged silicon-vacancy (SIV) centers, and achieve an enlarged GS splitting up to 1.8 THz. We further observe that the strain change due to local crystal structure modification can be reconfigured. Based on this effect, we demonstrate the nanoscale non-volatile

¹J. C. Wyant College of Optical Sciences, The University of Arizona, 1630 E. University Boulevard, Tucson, AZ 85721, USA. ²Department of Chemistry and Biochemistry, The University of Arizona, 1630 E. University Boulevard, Tucson, AZ 85721, USA. ³Sandia National Laboratories, Albuquerque, NM 87185, USA. ⁴Chandra Department of Electrical and Computer Engineering, The University of Texas at Austin, 2501 Speedway, Austin, TX 78712, USA.

✉ e-mail: xueyongzhou19@gmail.com; linran.fan@utexas.edu

classical memories using single SiV centers, which can operate up to 80 K temperature and support high-dimensional encoding. This work provides a promising method to control local strain of color centers, thus enhance the spin coherence time for quantum memories. The use of reconfigurable SiV centers as non-volatile classical memories also provides new opportunities for emerging applications such as photonic machine learning and neuromorphic computing^{18–20}.

Results

The electronic level structure of SiV centers is illustrated in the inset of Fig. 1a. Influenced by spin-orbit coupling and the Jahn-Teller effect, the optical excited and GS are split into two unique two-fold branches with frequency splittings around 259 GHz and 48 GHz, respectively^{21,22}. This specific level architecture results in four unique optical transitions in the zero-phonon line (ZPL), labeled as A, B, C, and D, respectively. The presence of external crystal strain further increases this splitting, forming the foundation for strain engineering aimed at reducing interactions with the acoustic phonon bath¹².

We introduced SiV centers via focused ion beam (FIB) implantation, previously demonstrated for a variety of group-IV color centers in both bulk and nanodiamonds^{23–27}. We use a home-built low-temperature confocal microscope to measure SiV centers. The photoluminescence (PL) spectrum is measured with cw pump at 532 nm. We can clearly observe four characteristic peaks, corresponding to the four optical transitions of SiV centers (Fig. 1a). The GS splitting can be determined from the frequency difference between characteristic peaks C and D. Before 532 nm pulsed laser irradiation, we extract a GS

splitting of 91 GHz, which is more than twice the zero-strain GS splitting (s1 in Fig. 1a). This is due to the strain introduced during ion implantation^{24,28}. The PL spectrum remains unchanged with the cw pump. Next, we use pulsed laser to irradiate the sample (pulse width 30 ps, repetition frequency 60 MHz, pulse energy 0.15 nJ). Then the PL spectrum is measured with cw pump again. After the pulsed laser irradiation, the location of all four characteristic peaks changes in the PL spectrum (s2 in Fig. 1a). In particular, the GS splitting is increased to 270 GHz, indicating that the strain perpendicular to the SiV symmetry axis is increased^{13,29}. The PL spectrum remains in the new state after the pulsed laser irradiation ends (see Supplementary Fig. 1). Therefore, the strain is maintained without keeping external fields.

Next, we verify that the change of the PL spectrum originates from different strain states of a single SiV color center instead of different SiV color centers. This is achieved by performing the second-order correlation measurement of the SiV color center pumped by the pulsed laser (Fig. 1b). A grating band-pass filter covering the wavelengths of the characteristic peak C in both PL spectra is used. While the PL spectra can change between the two states, the strong anti-bunching effect is observed at zero delay time. This confirms that there is only one SiV color center, and different PL spectra arise from different states of the same single SiV center.

We further observe that the characteristic peak C in two different states show a similar PL lifetime of 1.9 ns (Fig. 1c), which agrees with previously reported values^{22,30}. Then we examine the optical polarization of the characteristic peak C. As shown in Fig. 1d, both states demonstrated linear optical polarization, with a slight shift in the

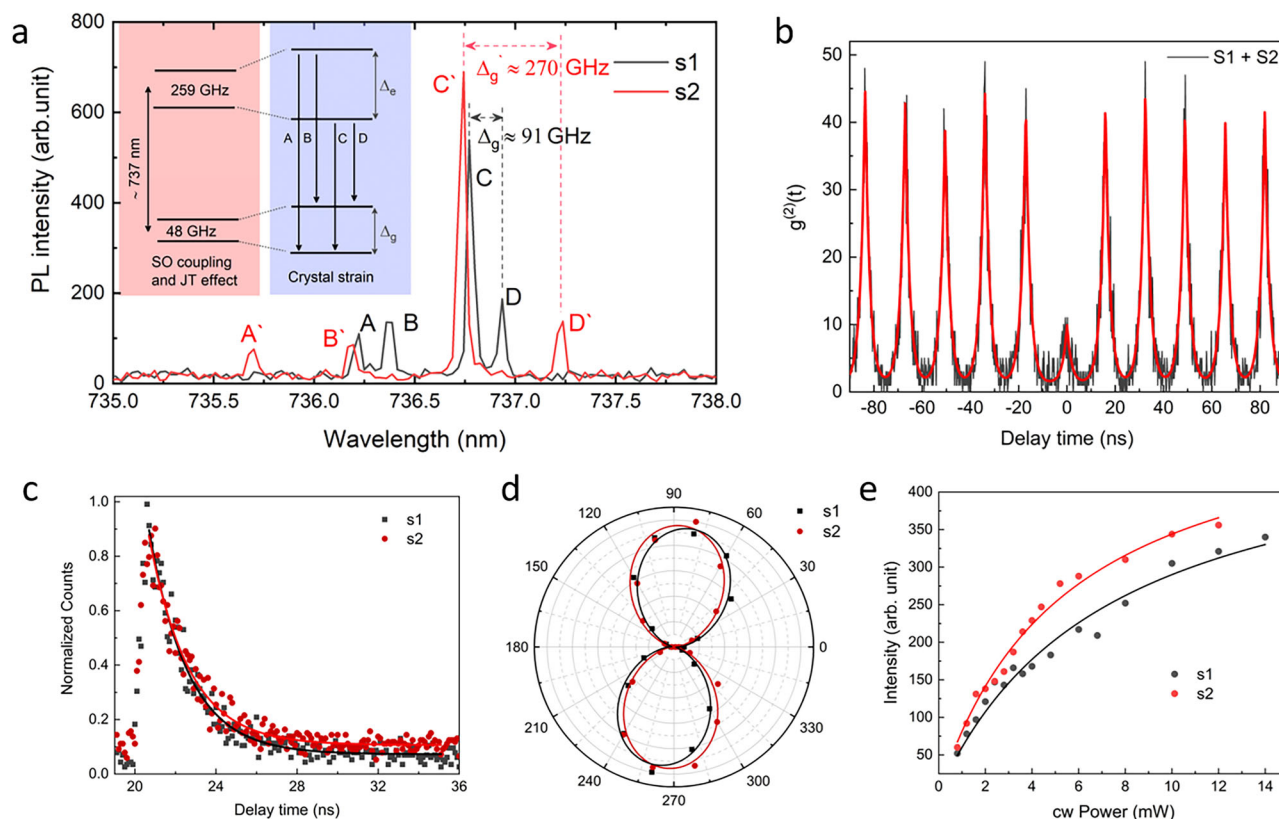


Fig. 1 | Optical characteristics of two states of a single SiV color center. **a** PL spectra before (s1) and after (s2) high-power pulsed laser irradiation. Both spectra exhibit the characteristic quartet of peaks (A, B, C, and D) unique to SiV centers. Inset: Simplified electronic level structure of SiV color centers in diamond. **b** The second-order correlation function measured under high-power pulsed laser excitation. A band-pass filter at the output covering the characteristic peak C location in

both s1 and s2 spectra is used. **c** PL lifetime before (s1) and after (s2) high-power pulsed laser irradiation. The pulsed pump for lifetime measurement is kept low to avoid the change of the SiV state. **d** Polarization profiles of the characteristic peak C before (s1) and after (s2) high-power pulsed laser irradiation. **e** PL signal saturation measured under cw laser excitation before (s1) and after (s2) high-power pulsed laser irradiation.

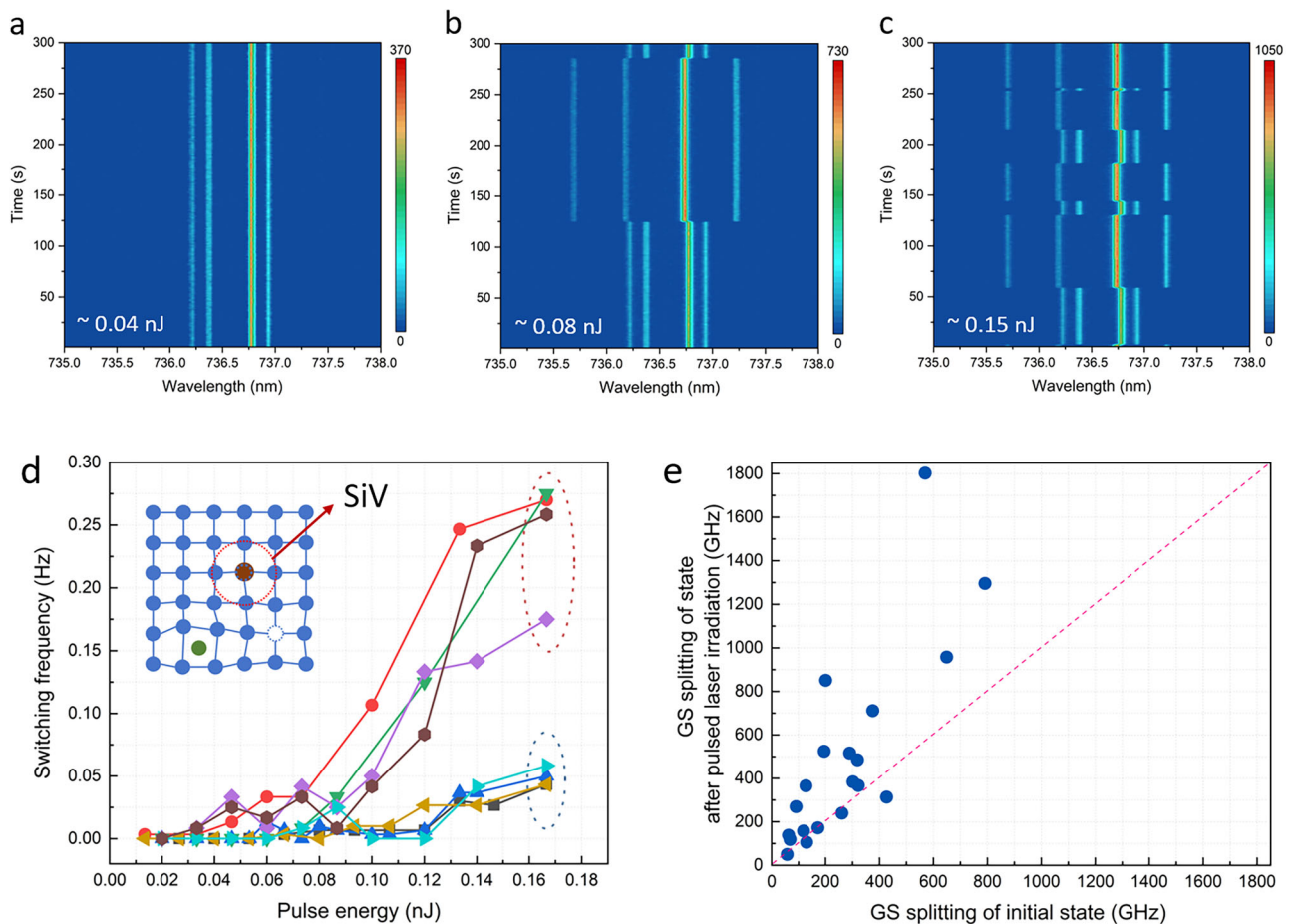


Fig. 2 | Time-dependent PL measurement and ground-state splitting. PL spectra of the SiV color center measured using pulsed pump with pulse energy (a) 0.04 nJ, (b) 0.08 nJ, and (c) 0.15 nJ respectively. **d** Pump power dependence of the switching frequency. Two different threshold powers are observed. Inset: schematic to show the vacancy (blue dashed empty circle) and self-interstitial (green solid circle)

defects. **e** Comparison of the GS splitting before and after high-power pulsed laser irradiation. The red dotted line visually separates emitters with increased GS splitting (above) from those with decreased splitting (below) after pulsed laser irradiation.

maximum polarization orientation by approximately 6 degrees. Furthermore, pump power saturation is observed for both states of the SiV color center, but with different saturation values of 7.4 mW and 5.6 mW, respectively (Fig. 1e). In addition, we emphasize here that the observed phenomena are distinctly different from charge state conversion in SiV centers, which would result in different emission wavelengths^{31,32}.

We further perform time-dependent PL measurement to explore the dynamics of the SiV state change (Fig. 2). With continuous high-power pulsed laser irradiation, the SiV color center randomly switches between the two stable states. Moreover, the switching frequency increases with the pulsed laser power. By measuring different SiV color centers, we observed two different types of the switching frequency dependence on the pulse energy (Fig. 2d). Threshold pulse energies are estimated of 0.043 ± 0.011 and 0.061 ± 0.012 nJ, respectively (see Supplementary Note 2). The ratio between the two threshold pulse energy matches the diffusion activation energy ratio between the vacancy and self-interstitial defects in diamond (2.3 eV and 1.6 eV respectively)^{33–35}. Therefore, we attribute the reconfiguration of SiV color centers to the lattice defect diffusion under high-power pulsed laser irradiation. The FIB implantation step to create SiV color centers inevitably introduces damages and distortion to the diamond lattice, which manifest in two forms including vacancies and self-interstitials (see the inset of Fig. 2d). This introduces the initial strain for SiV color centers. Under high-power laser irradiation, local diamond lattice can

be modified through the relaxation of photoionized electrons^{33–35}. The migration of defects between nearby lattice sites has the lowest energy barrier, thus highest occurrence probability. The change of the local diamond lattice causes the strain modification, which leads to the shift of characteristic peaks in the PL spectrum of SiV color centers. Given the energy limitation of our pulsed laser (0.17 nJ), the most commonly observed reconfiguration states are two. However, a few multi-state cases have also been noted (see Supplementary Fig. 3). We anticipate observing a greater variety of configurations with an increase in pulse energy³³. Furthermore, the diffusive behavior of both vacancies and interstitials is influenced by the unique strain fields surrounding individual SiV centers. Notably, in our experiments, approximately 52% of the strained SiVs exhibited this reconfiguration phenomenon.

We also observe that the GS splitting of SiV color centers tends to increase after the high-power pulsed laser irradiation (Fig. 2e). This is because the annealing step repairs the lattice damage and releases the strain in diamond lattice initially introduced during the FIB implantation²⁸. The high-power pulsed laser irradiation excites the local diamond lattice to a high-strain state with larger GS splitting. The amplitude of the GS splitting increase after the high-power pulsed laser irradiation is random as it depends on the distribution of diamond lattice defects. Still, we have observed GS splitting as large as 1.8 THz (see Supplementary Fig. 4). While the potential improvement on spin coherence time under high local strain requires future studies to verify, previous works have demonstrated that larger GS splitting can

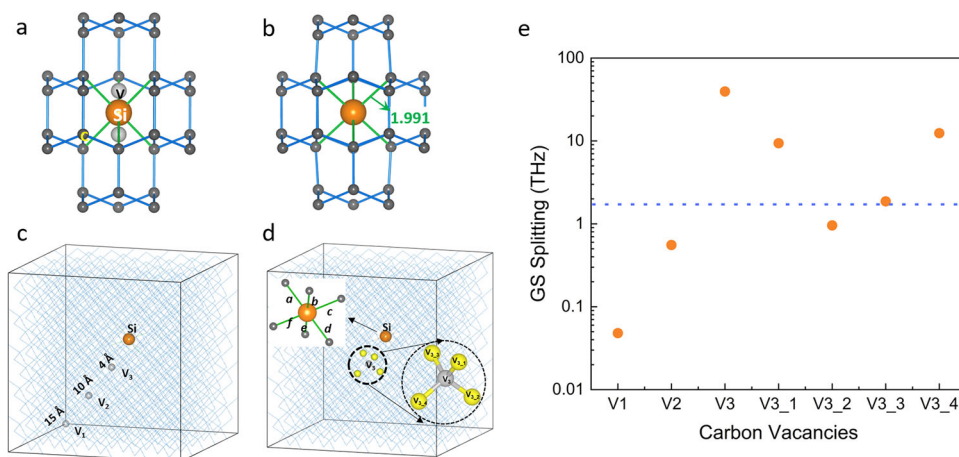


Fig. 3 | DFT calculation of GS splitting. **a** Schematic representation of the intrinsic SiV defect in diamond, the SiV is modeled by removing two adjacent carbon atoms and placing a silicon atom at the midpoint of the resulting carbon vacancies. **b** Optimized geometry of the SiV defect after structural relaxation, showing a calculated Si-C bond length of approximately 1.991 Å. **c** Schematic representation of

three carbon vacancies, V_i ($i = 1, 2, \text{ and } 3$), positioned at varying distances from the SiV. **d** Schematic representation of four carbon vacancies, $V_{3,x}$ ($x = 1, 2, 3, \text{ and } 4$), tetragonally coordinated to V_3 . The insert is depictions of the six Si-C bonds surrounding the SiV in the presence of V_i . **e** The GS splitting changing with the different carbon vacancies, the blue dash line represents the 1.8 THz.

suppress the phonon absorption then improve the spin coherence of the SiV centers^{11–14}. Furthermore, in some instances, the GS splitting of SiV color centers decreases following pulsed laser irradiation, indicating that local strain can be mitigated. This opens the possibility of completely eliminating local strain, ultimately enabling the creation of identical color centers.

Next, we developed a theoretical model and investigated the strain experienced by SiV centers due to nearby carbon vacancies in diamond using density functional theory (DFT) calculations based on first principles, without using any empirical parameters (details provided in Supplementary Note 5). The calculations were performed using a $5 \times 5 \times 5$ diamond supercell comprising 1000 carbon atoms. The intrinsic SiV defect was modeled by substituting two adjacent carbon atoms with one silicon atom placed at their midpoint (Fig. 3a), resulting in a structure of 998 carbon atoms and one silicon atom. After structural relaxation, the equilibrium Si-C bond length was determined to be approximately 1.991 Å without nearby defect perturbations (Fig. 3b). To examine the effect of additional carbon vacancies, we introduced an extra vacancy at three different locations (V_i , where $i = 1, 2, 3$), corresponding to 15, 10, and 4 Å away from the SiV center respectively (Fig. 3c). Then we calculated the six Si-C bond lengths surrounding the SiV in the presence of vacancies (Supplementary Note 5). The vacancy with a large distance from the SiV center (V_1 with 15 Å) only resulted in uniform changes in Si-C bond lengths, thus having negligible impact on ground state (GS) splitting. This indicates that the effective range for local strain engineering via nearby defects is limited to distances below 15 Å. On the other hand, vacancies closer to the SiV center (V_2 with 10 Å and V_3 with 4 Å) introduced significant distortion of the Si-C bonds surrounding the SiV center, thus large GS splitting.

Considering the four tetragonally coordinated carbon sites around the closest vacancy V_3 , we further investigated vacancy migration into four adjacent locations (denoted as V_{3-x} , $x = 1-4$, Fig. 3d). Vacancy migration substantially altered the local Si-C bond lengths and induced different strain distributions (Table 1). Given the high strain sensitivity (~ 1.3 PHz/strain) of the SiV electronic orbital states¹³, we calculated the resulting GS splitting for each of these vacancy positions (Fig. 3e; detailed calculations are shown in Supplementary Note 5). Our results indicated that a very close carbon vacancy (V_3) could induce GS splitting up to ~ 39.4 THz, while subsequent migration to adjacent sites can further change the GS splitting with

Table 1 | Strain values of the six Si-C bonds surrounding the SiV in the presence of $V_{3,1}$, $V_{3,2}$, $V_{3,3}$, $V_{3,4}$, and V_3 , expressed as percentages

Bond	$V_{3,1}$	$V_{3,2}$	$V_{3,3}$	$V_{3,4}$	V_3
a	-1.77%	-0.53%	-0.47%	-1.29%	-2.31%
b	-1.38%	-0.87%	-0.73%	-3.03%	-5.78%
c	3.55%	-0.55%	-0.54%	0.74%	1.26%
d	0.03%	-0.57%	-0.54%	-0.09%	0.50%
e	-2.49%	-0.13%	-0.11%	4.75%	13.36%
f	-2.33%	-0.48%	-0.47%	-1.76%	-2.91%

amplitudes ranging from 957 GHz to 12.4 THz. These findings underscore the high site sensitivity of local strain. Our computational results demonstrate vacancy migration as a promising mechanism to achieve significant local strain and thus enhance GS splitting in SiV centers. Experimentally, we observed a maximum GS splitting of approximately 1.8 THz, consistent with the DFT predictions. We also emphasize that experimentally characterizing larger splittings is challenging, as sufficiently large strain causes the disappearance of certain optical transition lines (A, B, D), leaving only line C visible, complicating accurate GS splitting measurements.

The unique reconfiguration capability of SiV color centers provides an ideal approach for non-volatile optical memory. The high-power pulsed laser irradiation serves as the writing operation, and the PL measurement under cw laser is used as the reading operation (Fig. 4a). The two states of SiV color centers are used to encode 0 and 1 respectively. Due to the stochastic nature of the writing process, we continuously monitor the PL spectrum during the writing operation. Once the target state is achieved, we turn off the pulsed laser. After the writing operation, we perform the reading operation with cw laser for verification. As shown in Fig. 4b, high-fidelity writing and reading can be achieved. No error is observed during the writing operation. Instead of the whole PL spectrum, we can simply use the PL intensity of the characteristic peak to distinguish 0 and 1 states (Fig. 4c). Contrast above 6 dB is achieved between 0 and 1 states. Such non-volatile memories have the potential to achieve high data storage densities, which are constrained primarily by the diffraction effects of the writing laser. However, the unique spectral signatures of different SiV centers

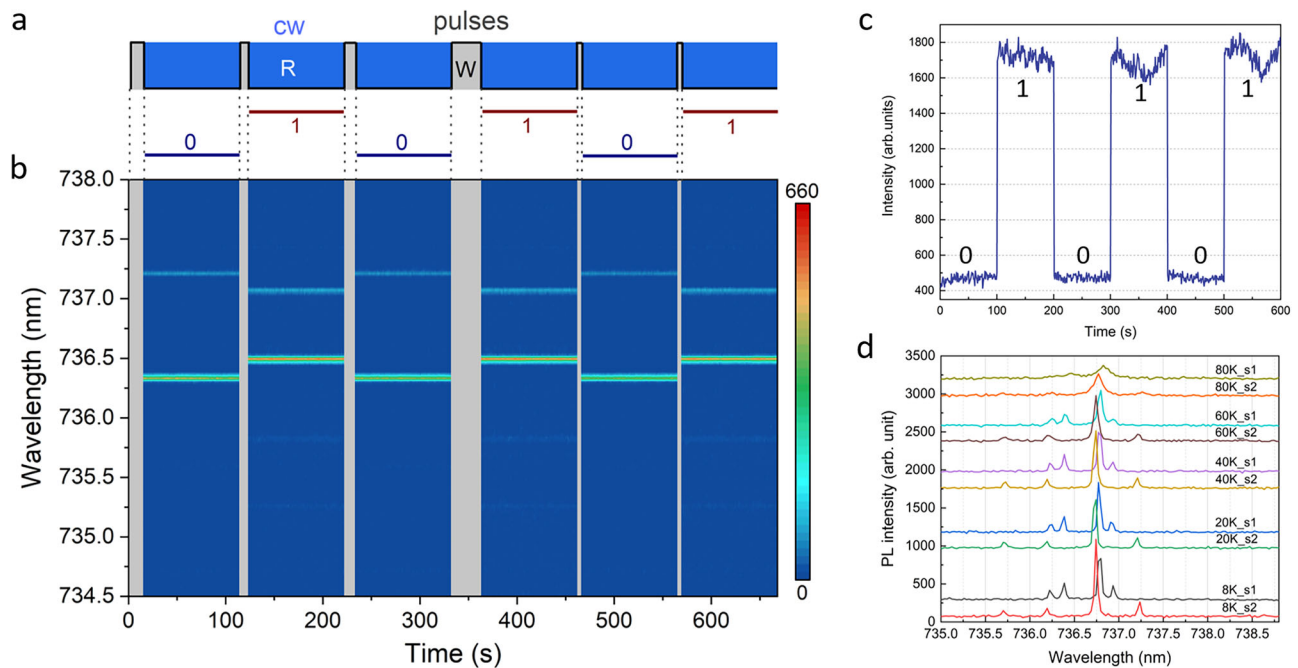


Fig. 4 | Non-volatile optical memory. **a** Writing and reading operations with pulsed and cw lasers respectively. **b** Time-dependent PL spectra to verify the writing operation. **c** PL intensity of the characteristic peak C. **d** PL spectra of the two strain states under different temperatures.

enable the deterministic writing of each SiV into a specific strain state within the same laser spot. This process is facilitated by real-time spectral monitoring, allowing us to exceed the diffraction limit of the writing laser^{36–39}. The non-volatile memory can function up to 80 K temperature, as the shift of the characteristic peak under strain reconfiguration is still larger than the linewidth (Fig. 4d). We expect to achieve a higher, or even ambient, functional temperature by selecting emitters with a large peak shift under local strain reconfiguration. The multiple configuration states, detailed in Supplementary Note 3, hold promise for facilitating high-dimensional data storage within non-volatile optical memories. These memories, based on SiV color centers, can deterministically write desired strain states while being monitored in real-time through spectral analysis.

Discussion

Conventional methods, such as suspended structures and membranes, can be classified as global strain engineering, as they involve applying external forces that bend or expose the entire diamond lattice to tune the target color centers. In contrast, the method presented here employs high-energy laser pulses to directly modify the surrounding lattice distribution, enabling local strain engineering. Given the exceptionally high elastic modulus of diamond (~1050 GPa), achieving significant strain for color center emitters through global approaches remains a formidable challenge. However, the local strain engineering method circumvents this limitation, offering the potential to induce larger strains with greater convenience. Furthermore, we propose a co-implantation strategy, where selected ions with larger atomic sizes and lower activation energies are implanted as impurity atoms near color centers⁴⁰. This approach introduces localized strain in a controllable manner, enhancing strain tunability and broadening the scope of potential applications. By integrating both local and global strain engineering methods, a broader tuning range can be achieved while maintaining high precision, making strain engineering a significantly more powerful tool for optimizing color centers.

Future works using high-efficiency nanostructures with enhanced collection efficiency and strong Purcell effects can enable detailed studies on the switching timescale between the different strain

states^{41–43}. The recent development of the direct laser writing technique for color center creation can also be leveraged to refine the laser irradiation condition for deterministic strain state reconfiguration^{44–48}. We anticipate that pulsed lasers with wavelengths longer than ZPL can also be used as the relaxation of photoionized electrons for strain state reconfiguration is introduced by multi-photon processes with broad absorption spectrum^{44,46}. This case is interesting as it may change the ground state splitting and optical transition without impacting electron spin states. It is also worth noting that this method can be applied widely to other solid-state systems such as color centers in silicon carbide and doped rare-earth ions.

In conclusion, our work has successfully developed an all-optical method to reconfigure single SiV color centers in diamond. This approach has unique advantages including no requirement of delicate nanostructures, maintaining strain without continuously applying external fields, and localized control of individual color centers at nanoscale. Through the power dependence of reconfiguration frequency, we identify the migration of local crystal lattice defects as the major dynamics for the reconfiguration of SiV color centers. Based on the reconfiguration capability, we further propose and demonstrate the use of SiV color centers in diamond as non-volatile optical memories. This method not only establishes a new paradigm for the direct manipulation of local strain in color centers for quantum photonics, but also heralds the development of ultra-compact optical data storage solutions for emerging classical applications such as photonic machine learning and neuromorphic computing.

Methods

Sample preparation and ion implantation

The electronic-grade diamond sample (Element 6) has a purity of approximately 1 ppb. The diamond sample was cleaned in 3:1 = H₂SO₄:H₂O₂ piranha solution for 20 min, to remove organic residues. To remove the strained surface, we etched the top 10 μm of the diamond sample with oxygen plasma. Subsequently, metal alignment markers were fabricated with the lift-off process. Focused ion beam implantation was executed using an A&D nanoImplanter—a specialized 100 kV focused ion beam system designed for high-precision

patterning and single ion implantation. The fluence of 28-Si^{2+} ions was set at 20 ions/spot with a spot pitch of $3\ \mu\text{m}$. With an ion beam energy of 70 keV, a penetration depth is $48 \pm 12\ \text{nm}$, simulated by SRIM⁴⁹. After FIB implantation, metal markers were removed using wet etchant. Then, the sample was annealed in an ultra-high vacuum environment of 1×10^{-8} Torr. The annealing step includes a temperature ramping to 400 °C over 4 h, followed by an increase to 800 °C for an additional 4 hours, and culminating at 1200 °C for a final 2 h duration. The heating rate was consistently maintained at 100 °C/h during both ramp-up and cool down phases. Post-annealing, the samples were treated with a triacid mixture comprising equal parts of H_2SO_4 , HNO_3 , and HClO_4 . This concoction was boiled and refluxed for 1.5 hours at 250 °C, aided by a water-cooled condenser. In the end, a final piranha cleaning step was implemented^{23,50}.

Optical Measurements

Optical measurements of SiV color centers in diamond were executed using a home-built confocal microscope, operating at temperatures approximately 8 K, in a Montana cryostat. A 100× objective lens (Olympus) with a numerical aperture of 0.85 was mounted inside the cryostat. The sample can be excited with either cw and pulsed 532 nm green lasers (pulse width 30 ps, repetition frequency 60 MHz). PL emitted from SiV color centers are collected by the same objective lens, separated from the pump with a dichroic mirror and a long-pass filter, before coupled into a single-mode fiber. PL emission was analyzed using a spectrometer, followed by silicon avalanche detectors. Photon correlation and lifetime measurement were implemented with a fiber-integrated Hanbury-Brown-Twiss (HBT) interferometer.

Data availability

All raw data generated during the current study are available from the corresponding authors upon request. Source data are provided with this paper.

References

- Bradac, C., Gao, W., Forneris, J., Trusheim, M. E. & Aharonovich, I. Quantum nanophotonics with group IV defects in diamond. *Nat. Commun.* **10**, 5625 (2019).
- Chen, D., Zheludev, N. & Gao, W.-B. Building blocks for quantum network based on group-IV split-vacancy centers in diamond. *Adv. Quantum Technol.* **3**, 1900069 (2020).
- Janitz, E., Bhaskar, M. K. & Childress, L. Cavity quantum electrodynamics with color centers in diamond. *Optica* **7**, 1232–1252 (2020).
- Pingault, B. et al. Coherent control of the silicon-vacancy spin in diamond. *Nat. Commun.* **8**, 15579 (2017).
- Debroux, R. et al. Quantum control of the tin-vacancy spin qubit in diamond. *Phys. Rev. X* **11**, 041041 (2021).
- Sukachev, D. D. et al. Silicon-vacancy spin qubit in diamond: a quantum memory exceeding 10 ms with single-shot state readout. *Phys. Rev. Lett.* **119**, 223602 (2017).
- Becker, J. N. et al. All-optical control of the silicon-vacancy spin in diamond at millikelvin temperatures. *Phys. Rev. Lett.* **120**, 053603 (2018).
- Bhaskar, M. K. et al. Experimental demonstration of memory-enhanced quantum communication. *Nature* **580**, 60–64 (2020).
- Stas, P.-J. et al. Robust multi-qubit quantum network node with integrated error detection. *Science* **378**, 557–560 (2022).
- Rosenthal, E. I. et al. Microwave spin control of a tin-vacancy qubit in diamond. *Phys. Rev. X* **13**, 031022 (2023).
- Guo, X. et al. Microwave-based quantum control and coherence protection of tin-vacancy spin qubits in a strain-tuned diamond-membrane heterostructure. *Phys. Rev. X* **13**, 041037 (2023).
- Sohn, Y.-I. et al. Controlling the coherence of a diamond spin qubit through its strain environment. *Nat. Commun.* **9**, 2012 (2018).
- Meesala, S. et al. Strain engineering of the silicon-vacancy center in diamond. *Phys. Rev. B* **97**, 205444 (2018).
- Assumpcao, D. R. et al. Deterministic creation of strained color centers in nanostructures via high-stress thin films. *Appl. Phys. Lett.* **123**, 241102 (2023).
- Ovartchaiyapong, P., Lee, K. W., Myers, B. A. & Jayich, A. C. B. Dynamic strain-mediated coupling of a single diamond spin to a mechanical resonator. *Nat. Commun.* **5**, 4429 (2014).
- Lee, K. W. et al. Strain coupling of a mechanical resonator to a single quantum emitter in diamond. *Phys. Rev. Appl.* **6**, 034005 (2016).
- Maity, S. et al. Spectral alignment of single-photon emitters in diamond using strain gradient. *Phys. Rev. Appl.* **10**, 024050 (2018).
- Genty, G. et al. Machine learning and applications in ultrafast photonics. *Nat. Photon.* **15**, 91–101 (2021).
- Shastri, B. J. et al. Photonics for artificial intelligence and neuromorphic computing. *Nat. Photon.* **15**, 102–114 (2021).
- Marković, D., Mizrahi, A., Querlioz, D. & Grollier, J. Physics for neuromorphic computing. *Nat. Rev. Phys.* **2**, 499–510 (2020).
- Müller, T. et al. Optical signatures of silicon-vacancy spins in diamond. *Nat. Commun.* **5**, 3328 (2014).
- Jahnke, K. D. et al. Electron-phonon processes of the silicon-vacancy centre in diamond. *New J. Phys.* **17**, 043011 (2015).
- Titze, M. et al. In situ ion counting for improved implanted ion error rate and silicon vacancy yield uncertainty. *Nano Lett.* **22**, 3212–3218 (2022).
- Sutula, M. et al. Large-scale optical characterization of solid-state quantum emitters. *Nat. Mater.* **22**, 1338–1344 (2023).
- Delegan, N. et al. Deterministic nanoscale quantum spin-defect implantation and diffraction strain imaging. *Nanotechnology* **34**, 385001 (2023).
- Harris, I. B. W. et al. Hyperfine spectroscopy of isotopically engineered group-iv color centers in diamond. *PRX Quantum* **4**, 040301 (2023).
- Xu, X. et al. Fabrication of single color centers in sub-50 nm nanodiamonds using ion implantation. *Nanophotonics* **12**, 485–494 (2023).
- Evans, R. E. et al. Narrow-linewidth homogeneous optical emitters in diamond nanostructures via silicon ion implantation. *Phys. Rev. Appl.* **5**, 044010 (2016).
- Sternschulte, H., Thonke, K., Sauer, R., Münzinger, P. & Michler, P. 1.681-eV luminescence center in chemical-vapor-deposited homoepitaxial diamond films. *Phys. Rev. B* **50**, 14554 (1994).
- Rogers, L. J. et al. Multiple intrinsically identical single-photon emitters in the solid state. *Nat. Commun.* **5**, 4739 (2014).
- Rose, B. C. et al. Observation of an environmentally insensitive solid-state spin defect in diamond. *Science* **361**, 60–63 (2018).
- Gardill, A. et al. Probing charge dynamics in diamond with an individual color center. *Nano Lett.* **21**, 6960–6966 (2021).
- Chen, Y.-C. et al. Laser writing of individual nitrogen-vacancy defects in diamond with near-unity yield. *Optica* **6**, 662–667 (2019).
- Davies, G., Lawson, S. C., Collins, A. T., Mainwood, A. & Sharp, S. J. Vacancy-related centers in diamond. *Phys. Rev. B* **46**, 13157 (1992).
- Twitchen, D. et al. The production and annealing stages of the self-interstitial (R2) defect in diamond. *Physica B* **273**, 644–646 (1999).
- Lian, C. et al. Photonic (computational) memories: tunable nanophotonics for data storage and computing. *Nanophotonics* **11**, 3823–3854 (2022).
- Chen, R. et al. Opportunities and challenges for large-scale phase-change material integrated electro-photonics. *ACS Photonics* **9**, 3181–3195 (2022).
- Alexoudi, T., Kanellos, G. T. & Pleros, N. Optical RAM and integrated optical memories: a survey. *Light Sci. Appl.* **9**, 91 (2020).

39. Ríos, C. et al. Integrated all-photonics non-volatile multi-level memory. *Nat. Photon.* **9**, 725–732 (2015).
40. Baron, Y. et al. Single G centers in silicon fabricated by co-implantation with carbon and proton. *Appl. Phys. Lett.* **121**, 081103 (2022).
41. Wan, N. H. et al. Large-scale integration of artificial atoms in hybrid photonic circuits. *Nature* **583**, 226–231 (2020).
42. Sipahigil, A. et al. An integrated diamond nanophotonics platform for quantum-optical networks. *Science* **354**, 847–850 (2016).
43. Chakravarthi, S. et al. Hybrid integration of gap photonic crystal cavities with silicon-vacancy centers in diamond by stamp-transfer. *Nano Lett.* **23**, 3708–3715 (2023).
44. Chen, Y.-C. et al. Laser writing of coherent colour centres in diamond. *Nat. Photon.* **11**, 77–80 (2017).
45. Kononenko, V. V. et al. Nitrogen-vacancy defects in diamond produced by femtosecond laser nanoablation technique. *Appl. Phys. Lett.* **111**, 081101 (2017).
46. Wang, X.-J., Fang, H.-H., Sun, F.-W. & Sun, H.-B. Laser writing of color centers. *Laser Photonics Rev.* **16**, 2100029 (2022).
47. Bharadwaj, V. et al. Femtosecond laser written photonic and microfluidic circuits in diamond. *J. Phys. Photonics* **1**, 022001 (2019).
48. Eaton, S. M. et al. Quantum micro-nano devices fabricated in diamond by femtosecond laser and ion irradiation. *Adv. Quantum Technol.* **2**, 1900006 (2019).
49. Ziegler, J. F. & Biersack, J. P. SRIM-2008, stopping power and range of ions in matter (2008).
50. Schröder, T. et al. Scalable focused ion beam creation of nearly lifetime-limited single quantum emitters in diamond nanostructures. *Nat. Commun.* **8**, 15376 (2017).

Acknowledgements

This work is supported in part by the NSF-ERC Center for Quantum Networks (EEC-1941583). X.N. was supported by the College of Science of the University of Arizona. We acknowledge the Research Data Center at the University of Arizona for providing high-performance computing resources. L.F. acknowledges the support from Coherent/II-VI Foundation. This work was performed, in part, at the Center for Integrated Nanotechnologies, an Office of Science User Facility operated for the U.S. Department of Energy (DOE) Office of Science. Sandia National Laboratories is a multimission laboratory managed and operated by National Technology and Engineering Solutions of Sandia, LLC, a wholly owned subsidiary of Honeywell International, Inc., for the U.S. DOE's National Nuclear Security Administration under contract DE-NA-0003525. The views expressed in the article do not necessarily represent the views of the U.S. DOE or the United States Government.

Author contributions

Y.X. and L.F. conceived the study. Y.X. conducted the experiments. M.T., S.S., Y.X., B.W., and L.Z. prepared and fabricated the sample. X.N. and Y.X. developed the DFT and calculation model. Y.X., L.Z., C.C., S.G., M.E., and L.F. participated in regular discussions of the results. All authors contributed to the drafting of the manuscript.

Competing interests

The authors declare no competing interests.

Additional information

Supplementary information The online version contains supplementary material available at <https://doi.org/10.1038/s41467-025-61384-y>.

Correspondence and requests for materials should be addressed to Yongzhou Xue or Linran Fan.

Peer review information *Nature Communications* thanks the anonymous reviewers for their contribution to the peer review of this work. A peer review file is available.

Reprints and permissions information is available at <http://www.nature.com/reprints>

Publisher's note Springer Nature remains neutral with regard to jurisdictional claims in published maps and institutional affiliations.

Open Access This article is licensed under a Creative Commons Attribution-NonCommercial-NoDerivatives 4.0 International License, which permits any non-commercial use, sharing, distribution and reproduction in any medium or format, as long as you give appropriate credit to the original author(s) and the source, provide a link to the Creative Commons licence, and indicate if you modified the licensed material. You do not have permission under this licence to share adapted material derived from this article or parts of it. The images or other third party material in this article are included in the article's Creative Commons licence, unless indicated otherwise in a credit line to the material. If material is not included in the article's Creative Commons licence and your intended use is not permitted by statutory regulation or exceeds the permitted use, you will need to obtain permission directly from the copyright holder. To view a copy of this licence, visit <http://creativecommons.org/licenses/by-nc-nd/4.0/>.

© The Author(s) 2025